electronics

MDPI

Article

Data-Driven Modeling of DC–DC Power Converters

Edgar D. Silva-Vera [1], Jesus E. Valdez-Resendiz [1,*], Gerardo Escobar [1], Daniel Guillen [1], Julio C. Rosas-Caro [2,*] and Jose M. Sosa [3]

[1] School of Engineering and Sciences, Tecnologico de Monterrey, Monterrey 64700, Mexico; a00833303@tec.mx (E.D.S.-V.); gerardo.escobar@tec.mx (G.E.); guillenad@tec.mx (D.G.)
[2] Facultad de Ingenieria, Universidad Panamericana, Alvaro del Portillo 49, Zapopan 45010, Mexico
[3] Laboratory of Electrical and Power Electronics, Instituto Tecnológico Superior de Irapuato, Irapuato 45010, Mexico; jose.sz@irapuato.tecnm.mx
* Correspondence: jesusvaldez@tec.mx (J.E.V.-R.); crosas@up.edu.mx (J.C.R.-C.)

Abstract: This article presents a data-driven methodology for modeling DC–DC power electronic converters. Using the proposed methodology, the dynamics of a converter can be captured, thereby eliminating the need for explicit theoretical modeling methods. This approach only requires the acquisition of fundamental measurements: currents through inductors and voltages across capacitors. The acquired data are used to construct a linear difference system, which is algebraically manipulated to form a state–space representation of the converter under analysis. Three DC–DC converter topologies were analyzed, and their resulting models were tested and compared with simulation data, yielding an average error deviation of approximately 2% for current signals and 4% for voltage signals, demonstrating precise tracking of the actual dynamics. The proposed data-driven methodology could simplify the implementation of adaptive control strategies in larger-scale solutions or in the interconnection of multiple converters.

Keywords: data-driven modeling; DC–DC power converter; converter modeling

check for updates

Citation: Silva-Vera, E.D.; Valdez-Resendiz, J.E.; Escobar, G.; Guillen, D.; Rosas-Caro, J.C.; Sosa, J.M. Data-Driven Modeling of DC–DC Power Converters. *Electronics* **2024**, *13*, 3890. https://doi.org/10.3390/electronics13193890

Academic Editors: Fernando Bento, Khaled Laadjal and Antonio J. Marques Cardoso

Received: 9 September 2024
Revised: 29 September 2024
Accepted: 30 September 2024
Published: 1 October 2024

Copyright: © 2024 by the authors. Licensee MDPI, Basel, Switzerland. This article is an open access article distributed under the terms and conditions of the Creative Commons Attribution (CC BY) license (https://creativecommons.org/licenses/by/4.0/).

1. Introduction

Power electronics DC–DC converters are electronic circuits implemented with semiconductor devices and energy storage elements such as capacitors and inductors to adjust the magnitude of the input DC voltage depending on the type of load and its requirements [1,2]. Some applications require a constant level at the output regardless of the disturbances that may occur, which can be due to variations in the input voltage, changes in the nominal output power, or the degradation of its energy storage elements [3].

According to [4], more than 500 prototypes of DC–DC converters have been developed and reported during the past six decades. These converters have been classified into six generations according to their characteristics and type of development:

- First generation: Classic converters;
- Second generation: Converters of multiple quadrants;
- Third generation: Switched component converters;
- Fourth generation: Soft switching converters;
- Fifth generation: Synchronous rectification converters;
- Sixth generation: Multi-element power resonant converters.

The development of new prototypes is mainly based on the direct modification of existing converters, the connection of multiple conversion stages, or combination and synthesis between circuits of first-generation converters [5,6]. For example, [7] provides a comprehensive review and evaluation of solid-state transformer (SST) prototypes in applications such as smart grids, railways, and offshore wind farms. It highlights future trends and the role of SSTs in transitioning to hybrid AC/DC electrical grids, along with

a detailed description of the system under study. Ref. [8] addresses the challenge of maximizing power extraction from photovoltaic (PV) systems while maintaining grid stability. The paper introduces a hybrid maximum power point tracking (MPPT) algorithm that combines perturb and observe (P&O) and incremental conductance (IC) methods to optimize PV performance. It uses two converters, coordinating MPPT for the PV plant and managing DC voltage control while reducing harmonic distortion on the AC side.

Due to the vast number of DC–DC converters reported in the literature, as well as the factors associated with their development, theoretical models that closely fit real-world systems tend to be complex [9–11]. There are two primary approaches to analyzing and modeling a converter: treating the converter as a sampled-data system [12] or as a continuous-time system. The continuous-time approach is generally preferred, as it facilitates the analysis of interactions with continuous passive components within the system. Among the methods that consider the converter as a continuous-time system are averaged modeling, small-signal modeling [13], and function-based models [14].

The most straightforward approach utilizes the moving average operator, or the state-space averaging technique, to smooth out the switching dynamics. However, this model is only effective for predicting converter behavior at frequencies below half of the switching frequency [15–17]. Two generalized averaging methods have been developed: the first is the Krylov–Bogoliubov–Mitropolsky (KBM) method, employed to solve the nonlinear differential equations that describe the system, particularly in cases where oscillatory behavior is present. This is achieved by expanding the solutions around a small perturbation parameter to obtain asymptotic solutions [18]. The second is multifrequency averaging modeling (MFA), which allows us to model both the steady-state behavior and transient responses of complex systems based on the harmonic evolution of the system's state variables [19].

The averaged small-signal model is useful for controller design, but its accuracy is questionable at high frequencies due to the elimination of high-frequency information by the moving average [20]. To improve modeling accuracy at high frequencies, multi-frequency small-signal models are introduced, and function-based models are proposed to address both constant and variable frequency modulation control [21,22].

Although averaged small-signal models and function-based models provide a single-input, single-output (SISO) linear input–output relationship, they fail to represent high-frequency interactions between multiple power converters. In certain scenarios, such as repetitive high-frequency load transients, multi-phase voltage regulators may exhibit beat frequency oscillations, which are not adequately explained by SISO models [23]. To address these limitations, cross-frequency models in the form of multiple-input, multiple-output (MIMO) representations have been proposed.

In addition to analytical methods, heuristic techniques such as neural networks have also been used to generate models that address the behavior of converters. In [24], the focus is on impedance identification based on neural networks for stability analysis in dual-side power supply railway systems. The method introduces a residual feedback neural network (ResFNN) combined with Shapley additive explanations (SHAP) to model the impedance of vehicles with a limited amount of data while maintaining high accuracy in predicting the impedance of traction converters. It also allows for the interpretation of the model's features by identifying the input parameters to the vehicle impedance, thus optimizing the training process. While this technique can be finely tuned, understanding how it makes decisions or what specific patterns it is learning can be complicated without additional interpretability techniques. There is also a dependency on training data, as the model may fail in certain scenarios if the data do not cover a sufficient range of operating conditions [24].

This work focuses on modeling a DC–DC converter as a black-box system using a data-driven approach. This approach employs estimation algorithms based on the collection and analysis of data. The proposed method aims to identify the system's behavior, which will be used to define a set of linear difference equations that provide an approximate system representation. This approach reconstructs the system's state trajectories from data without

relying on an explicit theoretical model. The contributions of this work can be summarized as follows:

1. We propose a state–space model representation based on a data-driven methodology, eliminating the need for prior knowledge of all converter parameters.
2. We provide a methodology capable of addressing the analysis of power electronics converters and determining state matrices.

The state–space model obtained allows for the characterization of key system properties, such as system dynamics, stability, and transient response. For example, this methodology can be useful in the design and analysis of magnetic systems, such as air–core bridge arm reactors used in DC transformers, which require accurate modeling of nonlinear electromagnetic fields [13,25].

The structure of the paper is as follows: Section 2 presents a study on the analysis and modeling of converters; Section 3 explains the methodology of the proposed data-driven method; Section 4 discusses the identification of the proposed systems and the results; finally, Section 5 presents our conclusions and future work.

2. DC–DC Converter Modeling Methods

Among the most common methods for modeling power electronic converters reported in the literature, the focus is on representing and analyzing the dynamic behavior of these devices to better understand their operation, optimize their design, and develop efficient control strategies. Depending on the method used for analysis, these approaches aim to capture nonlinearities, transient behavior, oscillations, harmonics generated by switching, optimization at specific operating points, and stability assessment. Table 1 presents some of the methods reported in the literature, along with their characteristics. A brief description of these methods is provided below.

Table 1. Summary of methods for power converters.

Modeling Method	Advantages	Limitations
State–Space Average Modeling [17,26,27]	Simplicity and ease of implementation. Suitable for stability and control analysis of converters. Requires fewer computational resources compared to more complex methods.	Does not adequately capture high-frequency effects. Limited to steady-state operation conditions or small perturbations around a fixed operating point.
Extended Harmonic Domain Modeling [28,29]	Provides a detailed view of harmonic generation and propagation. Allows for the study of interactions between different harmonics and the grid.	Large number of differential equations involved. Not suitable for modeling systems with rapid state changes, such as in fault conditions or severe disturbances.
Dynamic Phasor Modeling [30–32]	Enables the analysis of multi-frequency systems and rapid changes in the network. Offers good accuracy in representing the dynamics of converters.	Higher mathematical and computational complexity compared to average models. Requires a deep understanding of system behavior in the frequency domain.
Harmonic State–Space (HSS) Modeling [10,33–36]	Accurate frequency-domain description for power converters. Predicts frequency coupling interactions. Flexible for analyzing a selected range of harmonics.	Increased modeling complexity due to its higher order. Application may be limited by the lack of standardization in the development of HSS models for multi-converter systems.

2.1. State–Space Average Modeling

State–space average modeling (SSAM) is a widely used methodology for analyzing and designing power electronic converters, such as DC–DC converters. This approach involves representing the dynamic behavior of power converters in a mathematical model that describes the average values of currents and voltages over a switching period, thereby simplifying the analysis and design of control systems by focusing on their averaged dynamics rather than their high-frequency switching behaviors [16,17,26].

SSAM is based on the state–space representation of dynamic systems. In this approach, the state variables (such as inductor currents and capacitor voltages) are expressed as averaged quantities over one or multiple switching cycles. For power converters, the state–space model typically consists of differential equations that describe the relationship between the state variables, inputs (such as control signals or input voltage), and outputs (such as output voltage or current). These equations are averaged over a switching period to remove high-frequency switching content, resulting in a simplified model.

2.2. Extended Harmonic Domain Modeling

Extended harmonic domain (EHD) modeling is a framework used for analyzing and modeling power systems, particularly those involving voltage source converters (VSCs). This approach is designed to explicitly account for harmonic interactions within power systems by representing all harmonic components as individual state variables. The state–space representation of the system is extended to include these harmonic components, capturing both steady-state and dynamic behavior, which makes it more suitable for complex analyses than traditional averaged models [37].

In EHD modeling, each time-domain variable is represented by its complex Fourier coefficients, allowing for a detailed analysis of the harmonic interactions among various electrical quantities. This modeling approach supports both large-signal and small-signal analyses, enabling the study of both steady-state and dynamic behaviors of power electronic systems. This capability is particularly useful for analyzing issues such as harmonic stability, component design, and system optimization.

2.3. Dynamic Phasor Modeling

Dynamic phasor modeling is a technique used in power systems to represent the dynamic behavior of voltages and currents in systems that involve periodic or quasi-periodic signals. This modeling approach leverages time-varying Fourier series coefficients, known as dynamic phasors, to capture both the low-frequency and dynamic characteristics of these systems [30].

Dynamic phasors are based on the generalized averaging method. A waveform is observed over a specified interval, and its dynamic behavior is captured using its Fourier series coefficients, which vary with time, providing a compact representation of a signal that may include multiple harmonic components, capturing the essential dynamics while ignoring higher-frequency switching transients that are not of interest [30,31].

2.4. Harmonic State–Space Modeling

Harmonic state–space (HSS) modeling is a method employed to represent systems in power electronics applications, where time-domain state–space expressions are transformed into the frequency domain using Fourier coefficients [10]. This approach enables the consideration of the interaction of multiple harmonics in the frequency domain, allowing all harmonic components to be represented by their amplitude and phase angle. This transformation facilitates the determination of the direct current (DC) operating point of the converter, which is crucial for its analysis and design [10,34,35].

The mathematical formulation of HSS begins with a generic differential equation where the state, input, and output coefficient functions are periodic. An exponentially modulated periodic signal is used to ensure that the space of input and output signals remains consistent within the model. Additionally, the principle of harmonic balance is applied to relate the input harmonics to the output harmonics through harmonic transfer functions (HTFs) [38].

Finally, [39] deals with modeling the impedance characteristics of single-phase converters used in electric multiple units (EMUs) within vehicle-grid systems. The focus is on three main modeling methods: the direct-quadrature (DQ) model, the mirror-frequency impedance (MFI) model, and the harmonic state–space (HSS) model.

3. Metodology

In this section, a detailed analysis of the proposed methodology for a data-driven modeling approach focused on DC–DC power electronics converters will be conducted. The resulting model will take the form of a state–space representation, which helps us to determine the actual behavior of the analyzed converter. Figure 1 provides a general overview of the process to be followed for evaluating the system and constructing the state–space representation. This process is divided into two parts: part (a) focuses on retrieving and processing the necessary data for system evolution, while part (b) is centered around identifying system trajectories, fitting model equations, and simulating the resulting representation.

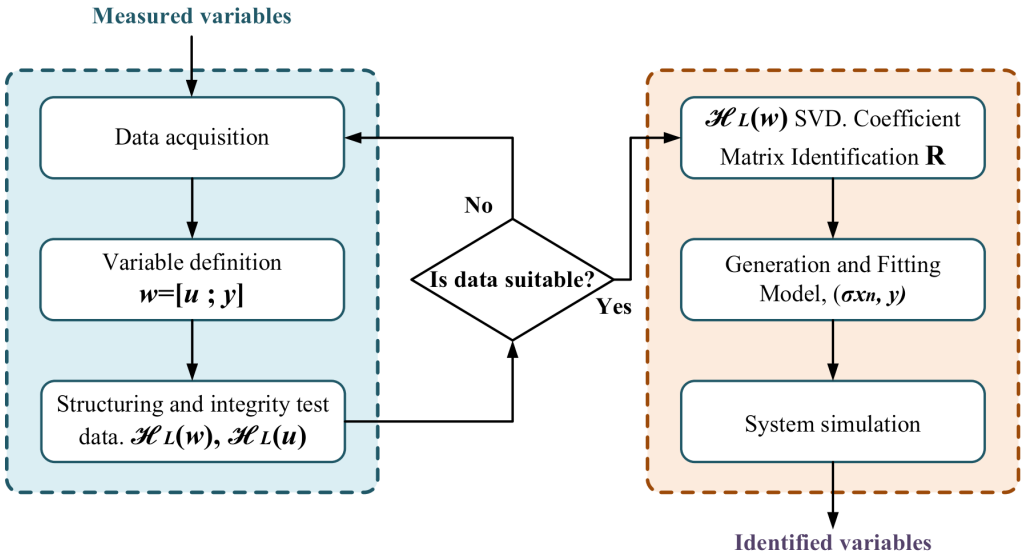


Figure 1. Block diagram of the data-driven parameter identification algorithm.

Data-Based System Modeling

Control systems are capable of autonomously adapting and modifying their behavior to optimize performance, enhance efficiency, and ensure safe operation by collecting and processing real-time data. The data-driven approach relies on the systematic collection of relevant data from the system being analyzed. During the data acquisition phase, it is essential to ensure that the sampling time t_s corresponds appropriately to the system's dynamics and that an optimal sampling window is established. The available measurement variable vector is composed of inputs $u = (u(1), u(2), u(3), \cdots, u(T))$ and outputs $y = (y(1), y(2), y(3), \cdots, y(T)$, where T correspond to the sequence of the series. Then, we can define a finite signal vector space as $\omega := \begin{bmatrix} u & y \end{bmatrix}^T$, which is classified and stored in a mapping discrete-time vector ω:

$$\omega(1), \omega(2), \omega(3), \ldots, \omega(T). \tag{1}$$

For linear, time-invariant, continuous-time systems, the system's behavior can be accurately represented through differential equations. A dynamical system is referred to as $\mathscr{C}$ if it is a linear vector subspace that encapsulates the system's behavior within $\mathbb{R}$ and remains invariant over time under the following conditions:

$$(\omega(\cdot) \in \mathscr{C}) \Longrightarrow (\omega(\cdot + t) \in \mathscr{C}) \forall \in \mathbb{R}. \tag{2}$$

This characteristic guarantees that the system's behavior stays unchanged over time [40,41]. Numerous systems can be modeled using differential equations and take the general form as follows:

$$f_1\left(\omega(t), \frac{d}{dt}\omega(t), \cdots, \frac{d^n}{dt^n}\omega(t)\right) = f_2\left(\omega(t), \frac{d}{dt}\omega(t), \cdots, \frac{d^n}{dt^n}\omega(t)\right). \tag{3}$$

In this context, f_1 and f_2 represent functions that describe the dynamics of the system. A specific representation of a linear, time-invariant, continuous-time differential system, $\mathscr{R}, \mathbb{R}^q, \mathscr{C}$, is defined by the solution set of a system of linear differential equations with constant coefficients [40]:

$$\mathscr{R}_0\omega(t) + \mathscr{R}_1\frac{d}{dt}\omega(t) + \mathscr{R}_2\frac{d^2}{dt^2}\omega(t) + \cdots + \mathscr{R}_n\frac{d^n}{dt^n}\omega(t) = 0. \tag{4}$$

Using constant matrices $\mathscr{R}_i \in \mathbb{R}^{q\times q}$ helps to encapsulate the information related to the system's state trajectories. Alternatively, if we treat the derivatives in Equation (4) as a finite difference approximation, the system can be expressed in the discrete domain as follows:

$$\mathscr{R}_0\omega(i) + \mathscr{R}_1\omega(i+1) + \mathscr{R}_2\omega(i+2) + \cdots + \mathscr{R}_n\omega(N) = 0, \tag{5}$$

where N is the maximum degree of the derivative, and $\mathscr{R}_i$ (with $i = 0, 1, \ldots, n$) contains the information corresponding to the variables of the system and will help to find the state representation [40,42]. Expression (5) can also be described as a kernel representation in terms of the shift operator σ; this operator can be applied to a function $f : \mathbb{Z}_+ \longrightarrow \mathbb{R}^q$ in the form $(\sigma f)(t) := f(t+1)$. This results in the following:

$$\mathscr{R}_0\omega + \mathscr{R}_1\omega\sigma + \mathscr{R}_2\omega\sigma^2 + \cdots + \mathscr{R}_n\omega\sigma^N = 0. \tag{6}$$

This allows for the algebraic manipulation of (6) and the factorization of ω. Additionally, by defining σ and $R(\sigma) : \mathscr{R}_0 + \mathscr{R}_1\sigma + \mathscr{R}_2\sigma^2 + \cdots + \mathscr{R}_N\sigma^N \in \mathbb{R}^{qxq}[\sigma]$, a kernel representation of the system can be obtained.

$$\begin{aligned} \begin{bmatrix} \mathscr{R}_0 & \mathscr{R}_1\sigma & \mathscr{R}_2\sigma^2 & \cdots & \mathscr{R}_n\sigma^N \end{bmatrix}\omega &= 0 \\ \mathscr{R}(\sigma)\omega &= 0, \end{aligned} \tag{7}$$

where N is the maximum degree of the shift operator σ. Note that to solve (7), it is necessary to find the value of the coefficient matrix $\mathscr{R}$. To achieve this, the following Hankel matrices are constructed:

$$\mathscr{H}_{L_{u,\omega}}(u) = \begin{bmatrix} a(1) & a(2) & \cdots & a(T-L+1) \\ a(2) & a(3) & \cdots & a(T-L+2) \\ \vdots & \vdots & \ddots & \vdots \\ a(L) & a(L+1) & \cdots & a(T) \end{bmatrix}, \tag{8}$$

where $L = length(u) + N$, with N being the number of states of the system, and a_i is associated with the input u or the signal vectors ω. The matrix $\mathscr{H}_{L_u}$'s purpose is to evaluate whether the measurement data allow for the complete characterization of the system's behavior. In other words, the goal is to determine if the signal is persistently exciting order L, which implies that the matrix has full row rank $\mathscr{H}_L(u)$ [43].

If the data are acceptable, a singular value decomposition (SVD) of $\mathscr{H}_L(w)$ with dimensions $m \times n$ is performed, which generates three simple matrices; thus, its SVD is expressed as follows:

$$\mathbf{U\Sigma V}^T = \mathscr{H}_L(\omega), \tag{9}$$

where $\mathbf{\Sigma} \in \mathbb{R}^{mxn}$ is a diagonal matrix that contains singular values and has the following form:

$$\mathbf{\Sigma} = \begin{bmatrix} \Sigma_i & 0 \\ 0 & 0 \end{bmatrix}, \tag{10}$$

with $\mathbf{U} \in \mathbb{R}^{m \times m}$ and $\mathbf{V}^T \in \mathbb{R}^{n \times n}$ orthogonal. If (9) is left-side multiplied by $\mathbf{U}^T$, the following is true:

$$\begin{bmatrix} \Sigma_i & 0 \\ 0 & 0 \end{bmatrix} \mathbf{V}^T = \mathbf{U}^T \mathscr{H}_L(\omega) = \begin{bmatrix} \beta \\ 0 \end{bmatrix}. \tag{11}$$

This means that $\mathbf{U}$ contains some values referred to as annihilators that make the values in ω zero; thus, it can be partitioned as $\mathbf{U} = \begin{bmatrix} U_1 & U_2 \end{bmatrix}$, where U_2 concentrates such annihilators. Moreover, from (7), it can be deduced that $\mathscr{R}(\sigma)$ is also an annihilator; thus, the following is true:

$$U_2 = \mathscr{R}, \tag{12}$$

with $\mathscr{R}$ of dimension $p \times q$, $p = length(y)$, and $q = length(y) \times L$. Once $\mathscr{R}$ has been identified, the next step consists of partitioning the matrix $\mathscr{R}$ as follows:

$$\mathscr{R} = \begin{bmatrix} \mathscr{R}_0 & \mathscr{R}_1 & \mathscr{R}_2 & \cdots & \mathscr{R}_{L-1} \end{bmatrix}. \tag{13}$$

From (7), and based on partition (13), the resulting equation is given by the following:

$$\mathscr{R}(\sigma)\omega = \mathscr{R}_0\omega + \mathscr{R}_1\sigma\omega + \cdots + \mathscr{R}_{L-1}\sigma^L\omega, \tag{14}$$

whose maximum delay degree is now constrained by the length of L.

From (14), space-mapping can be obtained through a technique called *shift and cut* [40], which applies a time displacement to obtain the system state variables as follows:

$$\begin{aligned} x_1 &= \mathscr{R}_1\omega + \mathscr{R}_2\sigma\omega + \cdots + \mathscr{R}_{L-1}\sigma^{L-1}\omega \\ x_2 &= \mathscr{R}_2\omega + \cdots + \mathscr{R}_{L-1}\sigma^{L-2}\omega \\ \vdots &= \vdots \\ x_{L-1} &= \mathscr{R}_{L-1}\omega. \end{aligned} \tag{15}$$

The resulting set of equations in (15) is used to approximate the state–space representation of the system. Applying a delay operator σ, and using (14), the resulting system can be expressed as follows:

$$\begin{aligned} \sigma x_1 &= -\mathscr{R}_0\omega \\ \sigma x_2 &= x_1 - \mathscr{R}_1\omega \\ \vdots &= \vdots \\ \sigma x_{L-1} &= x_{L-2} - \mathscr{R}_{L-2}\omega. \end{aligned} \tag{16}$$

Consider the output equation in (15) $y = \mathscr{R}\omega$, where $\omega = [uy]^T$. To ensure the operation is valid, $\mathscr{R}$ must be partitioned into $\mathscr{R}'_{p \times r}$ with $r = length(u)$ and $\mathscr{R}''_{p \times r}$. Notice that $\mathscr{R}''$ is always square. The output equation is obtained after developing the last equation of the state vector description (15), which yields the following:

$$\begin{aligned} x_{L-1} &= \mathscr{R}_{L-1}\omega \\ x_{L-1} &= \begin{bmatrix} \mathscr{R}'_{L-1} & \mathscr{R}''_{L-1} \end{bmatrix} \begin{bmatrix} u & y \end{bmatrix}^T \\ x_{L-1} &= \mathscr{R}'_{L-1}u + \mathscr{R}''_{L-1}y. \end{aligned} \tag{17}$$

The resulting expression for the output equation, in the form analogous to $y = Cx + Dx$ (in continuous time), can be recovered by multiplying the state vector x by the output matrix $C = \mathscr{R}''^{-1}_{L-1}$ and adding the contribution of the input u multiplied by the direct transmission matrix $D = \mathscr{R}'_{L-1}$, which yields the following:

$$y = \mathscr{R}''^{-1}_{L-1}x_{L-1} - \mathscr{R}''^{-1}_{L-1}\mathscr{R}'_{L-1}u. \tag{18}$$

This expression describes how states and inputs influence the output of the system. In summary, the state–space representation is given by (16) and (18).

Now, considering the state–space representation of a finite difference system given by

$$\begin{aligned} x(k+1) &= \mathbf{A}x(k) + \mathbf{B}u(k) \\ y(k) &= \mathbf{C}x(k) + \mathbf{D}u(k), \end{aligned} \tag{19}$$

matrices **A** and **B** can be computed as follows:

$$\mathbf{A} = \begin{bmatrix} 0 & 0 & 0 & \cdots & 0 & -\mathscr{A}_0 \\ \mathbf{I} & 0 & 0 & \cdots & 0 & -\mathscr{A}_1 \\ 0 & \mathbf{I} & 0 & \cdots & 0 & -\mathscr{A}_2 \\ \vdots & \vdots & \vdots & \ddots & \vdots & \vdots \\ 0 & 0 & 0 & \cdots & 0 & -\mathscr{A}_{L-3} \\ 0 & 0 & 0 & \cdots & \mathbf{I} & -\mathscr{A}_{L-2} \end{bmatrix}, \qquad \mathbf{B} = \begin{bmatrix} \mathscr{B}_0 \\ \mathscr{B}_1 \\ \mathscr{B}_2 \\ \vdots \\ \mathscr{B}_{L-3} \\ \mathscr{B}_{L-2} \end{bmatrix}, \tag{20}$$

where $\mathscr{A}_i = -\mathscr{R}''_i\mathscr{R}''^{-1}_{L-1}$ and $\mathscr{B} = \mathscr{A}_i\mathscr{R}'_{L-1} - \mathscr{R}'_i$ (with $i = 0, 1, 2, \ldots, L-2$). Also, identity matrix **I** has $q \times q$ dimensions. From (20), it is possible to approximate the eigenvalues and the time constant. Additionally, the system's controllability can be evaluated. Finally, matrices C and D are derived by the following:

$$\mathbf{C} = \mathscr{R}''^{-1}_{L-1}, \qquad \mathbf{D} = \mathscr{R}''^{-1}_{L-1}\mathscr{R}'_{L-1}. \tag{21}$$

4. DC–DC Power Converter Model Identification

Consider the system depicted in Figure 2, which consists of a DC–DC voltage source, an unknown load, and a DC–DC power electronics converter. The primary objective is to derive a state–space representation of the converter based on measurable variables, such as voltages and currents. Depending on the specific DC–DC converter topology, the number of variables may vary. In the case of voltages, these may include input voltage V_{in}, output voltage V_o, and/or the voltage across a capacitor V_{cx}, while for currents, these could be the input current I_{in}, the output current I_o, and/or the current through an inductor I_{Lx}.

In this work, we aim to obtain a model that approximately matches the real behavior of boost, SEPIC, and quadratic buck converters. The data for the variables of interest necessary to identify the coefficient matrix $\mathscr{R}$ were obtained from simulations conducted using the PSIM software for each of the aforementioned converters.

Table 2 presents the values for the passive components of the converters used in the simulations. A resistive load of $R_L = 22\ \Omega$ was applied to all three converters. Additionally, due to hardware limitations for computing and sampling, the switching and sampling frequencies were set to 100 kHz. Ref. [44] explores the advantages of designing DC–DC power converters to operate at very high frequencies (VHF) of hundreds of kilohertz, particularly those commonly used in converters from watts to several kilowatts in applications such as

battery chargers and renewable energy conditioning systems. Finally, the input voltage was fixed at 200 V.

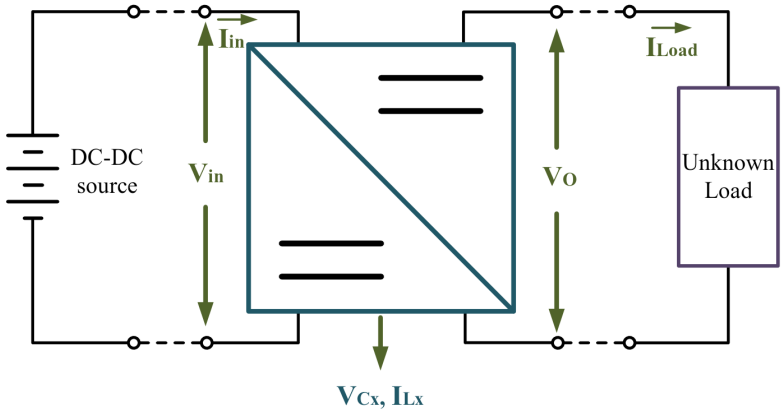


Figure 2. Unknown DC–DC power converter system for model identification.

Table 2. Capacitor and inductor values for the LC input filter of boost, SEPIC, and quadratic boost converters.

	LC Boost Converter	LC SEPIC Converter	Quadratic Buck Converter
L_{in}	100 µH	100 µH	1 mH
L_1	100 µH	100 µH	1 mH
L_2	-	100 µH	350 µH
C_{in}	10 µF	4.7 µF	10 µF
C_1	10 µF	10 µF	10 µF
C_2	-	10 µF	10 µF

Additionally, Table 3 presents the constants and eigenvalues for the analyzed converters, which were determined using both the mathematical models and the data-driven model. It is noteworthy that for the LC boost converter, the system order was reduced from fourth to second order when employing the data-driven model, and its time constant was smaller compared to the mathematical model. For the LC SEPIC and LC quadratic buck converters, the eigenvalues corresponding to the data-driven model were those closest to the imaginary axis. Lastly, the reported time constants represent the smallest and largest of the system, which are the key factors influencing the transient response and steady-state stability.

Table 3. Eigenvalues and time constant for the analyzed DC–DC converters.

	Boost Converter		SEPIC Converter		Quadratic Buck Converter	
	Physical Model	**Data-Driven Model**	**Physical Model**	**Data-Driven Model**	**Physical Model**	**Data-Driven Model**
λ_1	$0.0015 \pm 1.4604j$	$0.9992 \pm 0.0081j$	$0.001 \pm 1.4747j$	$0.4614 \pm 0.6092j$	$0.0037 \pm 1.3806j$	$0.1925 \pm 0.7621j$
λ_2	$0.0212 \pm 0.3417j$	-	$0.0159 \pm 0.3742j$	$0.6853 \pm 0.3472j$	$0.0087 \pm 0.6818j$	$0.4198 \pm 0.2802j$
λ_3	-	-	$0.006 \pm 0.7241j$	$0.4741 \pm 0.0971j$	$0.0104 \pm 1.0622j$	$0.4705 \pm 0.6676j$
τ_1	21.66 µs	6.37 µs	15.04 µs	8.29 µs	51.34 µs	74.89 µs
τ_2	92.33 µs	-	82.34 µs	13.15 µs	139.25 µs	143.25 µs

It should be emphasized that the identification conducted for these converter models and their comparison is based on the averaged model. Behaviors resulting from switching

and small-signal perturbations are excluded from this identification, primarily to enable a comparison between already identified models and those developed using data-driven methodology. This does not imply that the methodology for identifying models under those conditions is invalid.

Additionally, to assess the accuracy of the identified models, the quantitative metric of root mean square error (RMSE) has been implemented. This metric allows for better evaluation of the model's performance in the presence of relatively large deviations from the actual values. Furthermore, if the model exhibits high variability in its estimation errors, the RMSE will reflect this instability, enabling the detection of inconsistencies in the model's performance.

An important aspect to highlight during both the identification process and the evaluation of the identified model is the idealization of the converter's operation. This assumption results in measurements free from internal and external disturbances, thereby avoiding discrepancies when tracking the actual behavior of the system.

In general, such discrepancies increase estimation bias in the presence of significant noise, leading to errors and reduced precision. In any real-world application, it is necessary to condition the measured signals to ensure optimal quality for post-processing in digital systems [45,46].

4.1. LC Input Boost Converter

For the data-based model identification of the LCL boost converter, as depicted in Figure 3, the variables utilized are the output voltage $V_o = y_1$ and the current through the inductor L_1, $I_{L1} = y_2$, which are defined as the outputs of the algorithm. The input is defined as the duty cycle d.

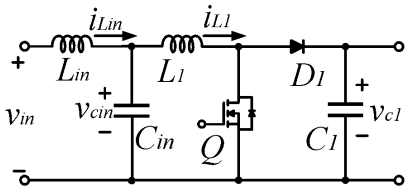


Figure 3. Electrical circuit for the LCL boost converter.

Moreover, to excite the outputs, the duty cycle was varied between 0.4, 0.55, and 0.4 in an exponential manner with intervals of 62.5 ms. This variation ensures a transition in the output power between 5 and 9 kW, thereby providing a reasonable change in the input variables and facilitating the identification of the coefficient matrix $\mathscr{R}$.

$$\begin{aligned} x_1(k+1) &= -R_0\omega \\ y &= R_1^{''-1}x_1 - R_1^{''-1}R_1^{'}u. \end{aligned} \tag{22}$$

The difference equations system presented in (22) allow for an approximate identification of the LCL boost converter model. This can be observed in Figure 4, where the voltage V_o and current I_1 are compared for simulation data and the estimate provided by the data-based model. For both models, the natural oscillatory behavior of the converter is observed, highlighting that the data-based model exhibits a greater magnitude of this behavior. Additionally, the time it takes for the current and voltage signals to stabilize is much longer compared to what is observed in the electrical model. In the case of the output voltage, it is also noted that the initial transient has a much smaller magnitude.

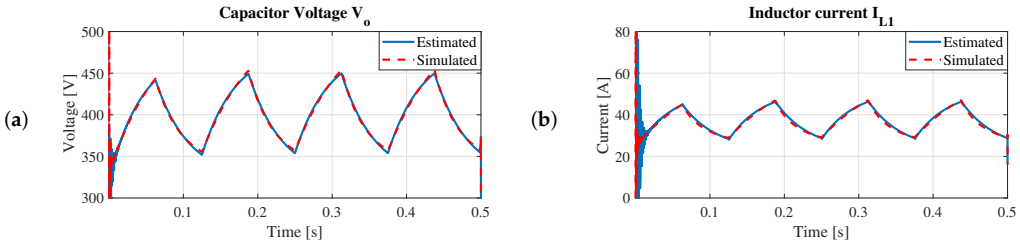


Figure 4. LCL boost identified vs simulated waveforms (**a**) capacitor voltage V_o and (**b**) inductor current I_{L1}.

Additionally, (23) presents a comparison between the state matrix **A** derived from the mathematical analysis [47] $\mathbf{A}_{1m}$ and that calculated from the state–space representation $\mathbf{A}_{1d}$. Furthermore, in this case, the system order is reduced from a fourth-order system to a second-order system.

$$\mathbf{A}_{1d} = \left[-\mathbf{R}_0''\mathbf{R}_1''^{-1}\right] \qquad \mathbf{A}_{1m} = \begin{bmatrix} 0 & 0 & -1 & 0 \\ 0 & 0 & 1 & -u^* \\ 1 & -1 & 0 & 0 \\ 0 & u^* & 0 & -1/R \end{bmatrix}. \tag{23}$$

Figure 5 illustrates the deviation between the simulated and estimated measurements for the voltage V_o and the current I_{L_1}. In both cases, it can be observed that as more observations are made, the error decreases. Additionally, regions where the error tends toward zero can be identified. For example, when comparing V_o RMSE error e_{VCO} with its magnitude, it is determined that the model begins to diverge in the linear regions of the measured parameters, while the error tends to zero as the perturbation increases.

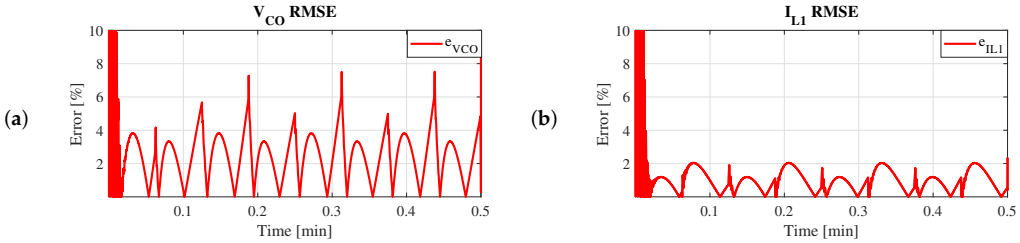


Figure 5. LCL boost. Error between the simulated electrical model and data-driven identified model for (**a**) capacitor voltage V_o and (**b**) inductor current I_{L1}.

4.2. LCL SEPIC Converter

The circuit used during the simulation of the LCL SEPIC converter is depicted in Figure 6. The parameters of interest in this topology correspond to the capacitor voltage C_2 and the current through inductors L_1 and L_2, which are denoted as $V_o = y_1$, $I_{L1} = y_1$, and $I_{L2} = y_3$, respectively. The input remains defined as the duty cycle $u = d$.

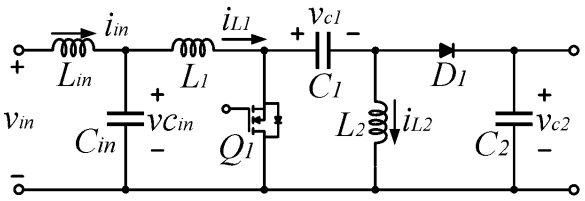


Figure 6. Electrical circuit for the LCL boost converter.

For the duty cycle, a constant value of $d = 0.5$ was assumed for the first 100 ms, followed by an exponential transition of 0.06 every 100 ms. This approach ensures that the converter operates in boost mode, preventing the model from switching between buck and

boost behaviors. As a result, the coefficient matrix $\mathscr{R}$ captures a more consistent behavior, leading to a model that closely approximates real-world performance.

The system of equations describing the behavior of this converter is presented in (24). Note that, unlike the LCL boost converter, the state equations now increase to three.

$$\begin{aligned} x_1(k+1) &= -R_0\omega \\ x_2(k+1) &= x_1(k) - R_1\omega \\ x_3(k+1) &= x_2(k) - R_2\omega \\ y &= R_3''^{-1}x_3 - R_3''^{-1}R_3'u. \end{aligned} \tag{24}$$

Figure 7 shows a comparison between the converter's output signals and those generated by the identified model. The blue line represents the estimated values, while the orange dashed line corresponds to the simulation signals. It can be observed that the estimated variables eliminate the initial transient response inherent to the voltage and current dynamics. Additionally, although the behavior of these variables is closely followed, a slight error exists between the two signals.

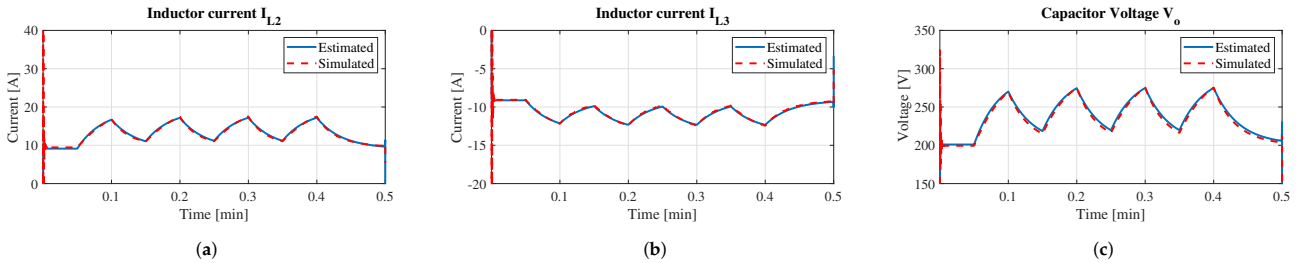


Figure 7. LCL SEPIC identified vs simulated waveforms (**a**) inductor current I_{L2}, (**b**) inductor current I_{L3}, and (**c**) capacitor voltage V_o.

Equation (25), a comparison is provided between the state matrix derived from a mathematical analysis (A_{2m}) and the one obtained from the state–space representation (A_{2d}). It should be noted that A_{2d} has dimensions of 9×9, primarily due to the increase in linear difference equations proposed to emulate the system's state behavior.

$$\mathbf{A}_{2d} = \begin{bmatrix} 0_{3\times3} & 0_{3\times3} & [-\mathbf{R}_0''\mathbf{R}_3''^{-1}]_{3\times3} \\ \mathbf{I}_{3\times3} & 0_{3\times3} & [-\mathbf{R}_1''\mathbf{R}_3''^{-1}]_{3\times3} \\ 0_{3\times3} & \mathbf{I}_{3\times3} & [-\mathbf{R}_2''\mathbf{R}_3''^{-1}]_{3\times3} \end{bmatrix} \mathbf{A}_{2m} = \begin{bmatrix} 0 & 0 & 0 & -1 & 0 & 0 \\ 0 & 0 & 0 & 1 & u^*-1 & u^*-1 \\ 0 & 0 & 0 & 0 & u^* & u^*-1 \\ 1 & -1 & 0 & 0 & 0 & 0 \\ 0 & 1-u^* & -u^* & 0 & 0 & 0 \\ 0 & 1-u^* & 1-u^* & 0 & 0 & -1/R \end{bmatrix}. \tag{25}$$

Finally, Figure 8 shows the RMSE error for the LCL SEPIC data-driven model. Calculated error corresponds to the deviation between the estimates and the simulated values. These relate to the error in the current of inductors L_1 and L_2 and the voltage across the output capacitor C_2, corresponding to e_{IL2}, e_{IL3}, and e_{Vo}. It can be observed that the model shows better tracking for the currents, which may suggest that the deviation not only depends on the type of excitation in the input variables but also on the magnitude of the deviation observed in the output variables.

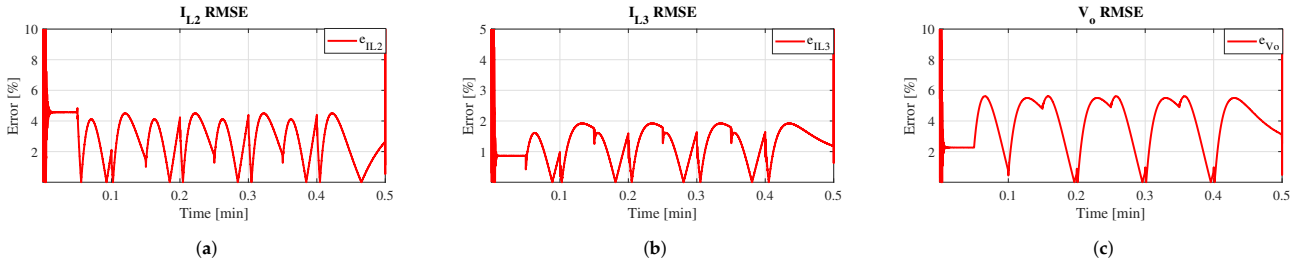


Figure 8. LCL SEPIC. Error between the simulated electrical model and data-driven identified model for (**a**) inductor current I_{L2}, (**b**) inductor current I_{L3}, and (**c**) capacitor voltage V_o.

4.3. LC Input Quadratic Buck Converter

The final model to be identified corresponds to the quadratic buck converter, as illustrated in Figure 9. Parasitic elements were considered in the inductors with a resistance value of $R_{L_x} = 0.4\ \Omega$. The variables to be considered for the model derivation are as follows: the voltage across capacitor C_1, denoted as $V_{C1} = y_1$; the output voltage $V_o = y_2$; the currents through inductors L_1 and L_2, which are represented as $I_{L_1} = y_3$ and $I_{L_2} = y_4$, respectively. The duty cycle input d is varied exponentially within the range of $\Delta d = \pm 0.12$ over periods of 100 ms.

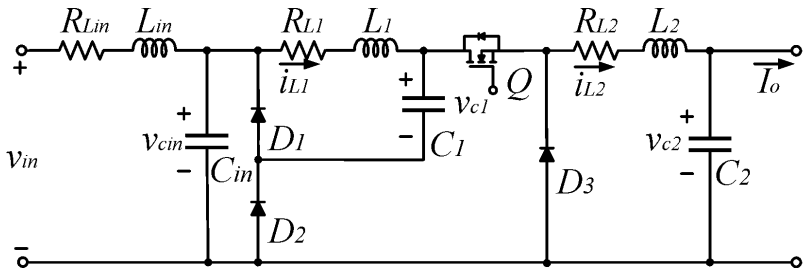


Figure 9. Electrical circuit for the LC input filter quadratic buck converter.

The identification of the coefficient matrix $\mathscr{R}$ for this converter results in the system of equations presented in (26), which, for this system, includes four state trajectory equations.

$$\begin{aligned} x_1(k+1) &= -R_0\omega \\ x_2(k+1) &= x_1(k) - R_1\omega \\ x_3(k+1) &= x_2(k) - R_2\omega \\ x_4(k+1) &= x_3(k) - R_3\omega \\ y &= R_4^{''-1}x_4 - R_4^{''-1}R_4^{'}u. \end{aligned} \tag{26}$$

In Figure 10, the output variables generated by the proposed model (solid blue line) are compared with those obtained through simulation (dotted line). It is observed that the model adequately tracks the converter's outputs, although it exhibits discrepancies in approximating the magnitude near the maximum and minimum limits. Additionally, it is observed that the initial oscillatory behavior is completely mitigated in the data-based model for both currents and voltages. Finally, the components due to switching are mitigated, although they are still present.

Finally, (27) provides the state–space matrices for both the data-driven state–space representation (A_{3d}) and the theoretical model derived from averaged analysis (A_{3m}).

$$\mathbf{A}_{3d} = \begin{bmatrix} 0_{4\times4} & 0_{4\times4} & 0_{4\times4} & [-\mathbf{R}_0''\mathbf{R}_4''^{-1}]_{4\times4} \\ \mathbf{I}_{4\times4} & 0_{4\times4} & 0_{4\times4} & [-\mathbf{R}_1''\mathbf{R}_4''^{-1}]_{4\times4} \\ 0_{4\times4} & \mathbf{I}_{4\times4} & 0_{4\times4} & [-\mathbf{R}_2''\mathbf{R}_4''^{-1}]_{4\times4} \\ 0_{4\times4} & 0_{4\times4} & \mathbf{I}_{4\times4} & [-\mathbf{R}_3''\mathbf{R}_4''^{-1}]_{4\times4} \end{bmatrix}$$

$$\mathbf{A}_{3m} = \begin{bmatrix} 0 & 0 & 0 & -1 & 0 & 0 & 0 \\ 0 & 0 & 0 & u^* & -1 & 0 & 0 \\ 0 & 0 & 0 & 0 & u^* & -1 & 0 \\ 1 & -u^* & 0 & 0 & 0 & 0 & 0 \\ 0 & 1 & -u^* & 0 & 0 & 0 & 0 \\ 0 & 0 & 1 & 0 & 0 & -1/R & 0 \\ 0 & 0 & 0 & 0 & 0 & 1 & 0 \end{bmatrix}. \quad (27)$$

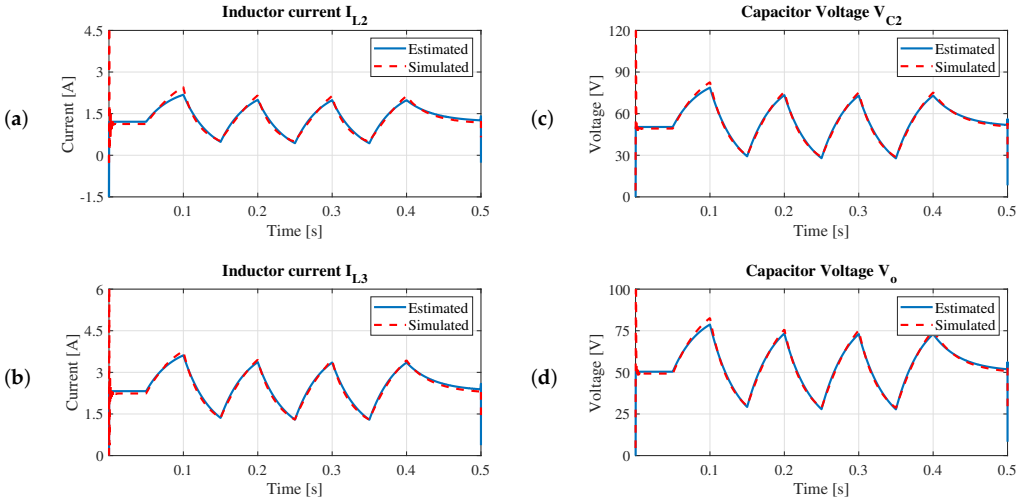


Figure 10. Quadratic buck converter identified vs. simulated waveforms: (**a**) inductor current I_{L2}, (**b**) inductor current I_{L3}, (**c**) capacitor voltage V_{C2}, and (**d**) capacitor voltage V_o.

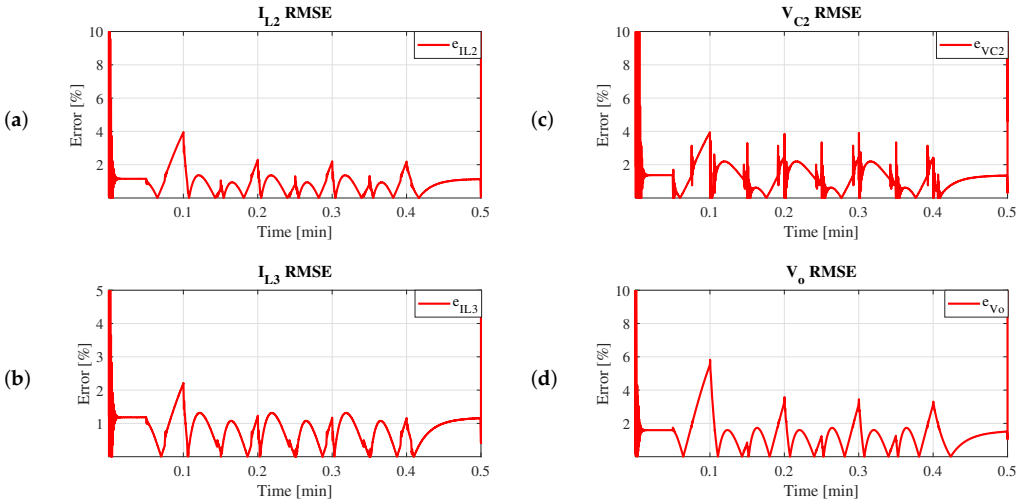


Figure 11. LC quadratic buck. Error between the simulated electrical model and data-driven identified model for (**a**) inductor current I_{L_2}, (**b**) inductor current I_{L_3}, (**c**) capacitor voltage V_{C_2}, and (**d**) capacitor voltage V_o.

Figure 11 shows the calculated RMSE error between the estimates and the simulated values. These relate to the error in the current of inductors L_1 and L_2, as well as the voltage

across capacitor C_1 and output capacitor C_2, corresponding to e_{IL2}, e_{IL3}, e_{VC2}, and e_{Vo}. It can be observed that the model shows better tracking for the currents.

5. Model Validation

To validate the system of equations for the state–space representations obtained for each converter, a simulation was conducted by varying the input u, i.e., the duty cycle d. This variation followed a step-like change with $\Delta d = 0.01$ every 50 ms. For this validation, the sampling frequency was reduced to 10 kHz, which does not affect the process, as the identification of the coefficient matrix $\mathscr{R}$ is no longer performed.

5.1. LC Input Boost Converter

Figure 12 presents the plots for the output voltage V_o and the inductor current I_{L1} of the *LCL* boost converter. Both estimations exhibit oscillatory behavior at the start, with the estimated signals showing a higher magnitude. Additionally, this oscillatory behavior is also observed during duty cycle transitions. It can be seen that the data-driven model is capable of tracking the trajectory of the real system. An error analysis is required to quantify the deviation between the estimation and the simulation.

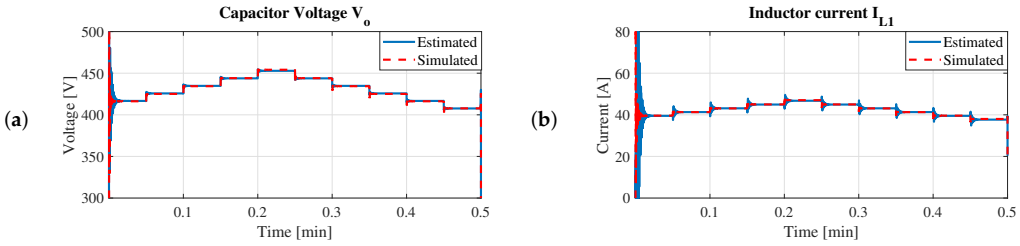


Figure 12. Simulated and estimated waveform for a step-like change d: (**a**) converter output voltage V_o and (**b**) inductor current I_{L1}.

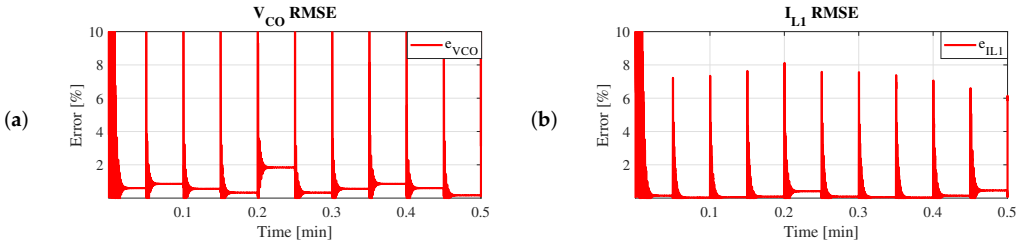


Figure 13. For the data−driven identified model, error between simulated and estimated signals (**a**) V_o and (**b**) inductor current I_{L1}.

To evaluate the model's accuracy under conditions different from those used during its identification, Figure 13 shows the RMSE error for current I_{L_1} in (b) and for output voltage V_o in (a). During steady-state periods, the magnitude of these errors stays below an average of 1%. However, during transient phases resulting from changes in the input signal d, errors of up to 10% are observed. This is attributed to the minimal transient response in the estimated signal produced by the data-driven model.

5.2. LCL SEPIC Converter

The plots presented for the LCL SEPIC converter in Figure 14 correspond to the estimated currents in I_{L_1} and I_{L_2}, as well as the output voltage. The signals are compared between the state–space representation (dotted line) and the simulation results. It can be observed that, in this case, the estimation of the output variables does not exhibit oscillatory or transient behavior due to the step transition of the duty cycle. This is attributed to the augmentation of the system's state equations, which allows the hidden states of the model to function as a filter for high frequencies.

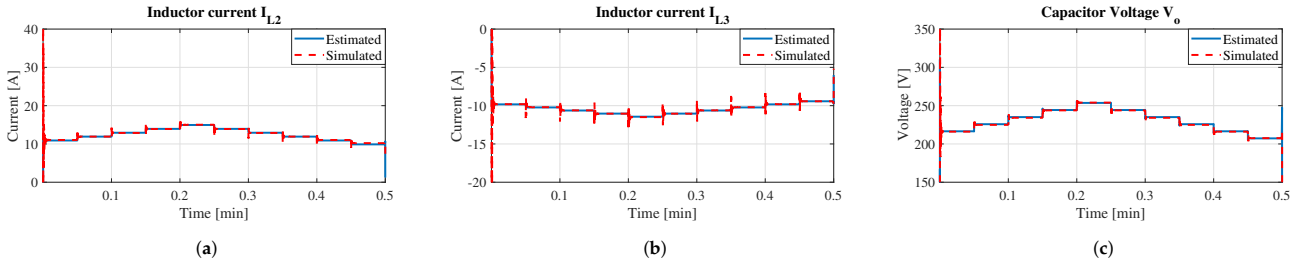


Figure 14. Simulated and estimated waveform for a step−like change d converter: (**a**) inductor current I_{L1}, (**b**) inductor current I_{L3}, and (**c**) capacitor voltage V_o.

To assess the model's accuracy under conditions different from those used for its identification, Figure 15 presents the RMSE error for currents $I_{L_{2,3}}$ in (a) and (b), as well as for output voltage V_o in (c). The magnitude of these errors remains below an average of 1% during steady-state periods. However, during transient phases caused by changes in the input signal d, errors of up to 10% are observed. This is due to the minimal transient response in the estimated signal generated by the data-driven model.

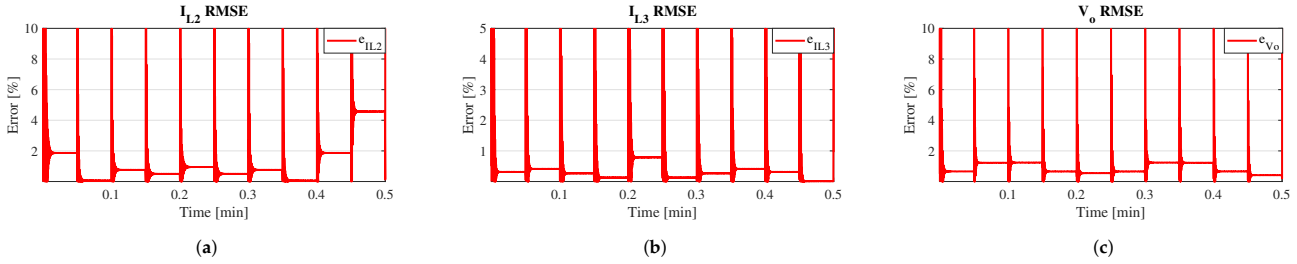


Figure 15. For the data−driven identified model, error between simulated and estimated signals: (**a**) inductor current I_{L1}, (**b**) inductor current I_{L3}, and (**c**) capacitor voltage V_o.

5.3. LC Input Quadratic Buck Converter

In Figure 16, the estimated and simulated graphs for the quadratic buck converter are shown, corresponding to the currents in I_{L1} and I_{L2}, as well as the voltages in V_{C1} and V_o. It can be observed that the transients in the estimated signals have been almost completely attenuated. This is due to the increase in the order of the linear difference equations in the obtained model. This may indicate that, as the number of equations increases for a system, the transient behavior may not be represented optimally.

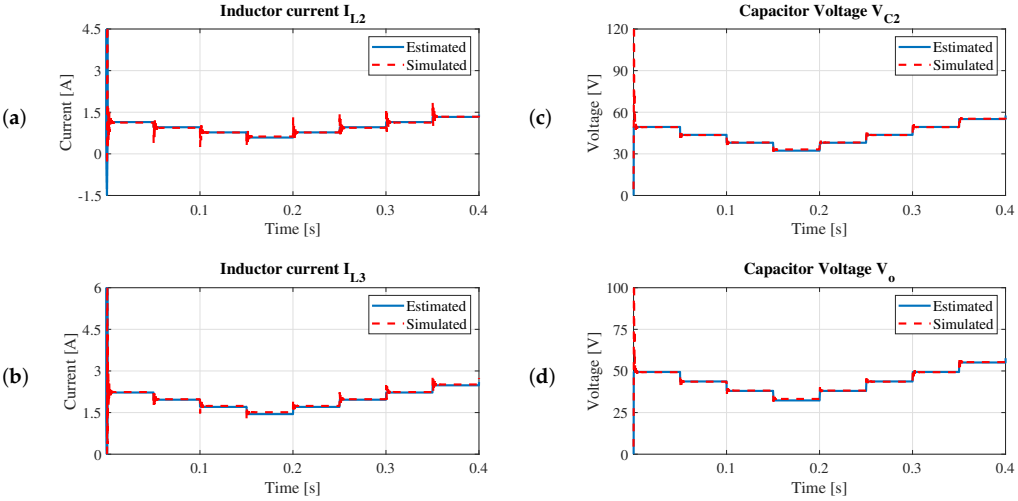


Figure 16. Simulated and estimated waveform for a step−like change d converter: (**a**) inductor current I_{L2}, (**b**) inductor current I_{L3}, (**c**) capacitor voltage V_{C2}, and (**d**) capacitor voltage V_o.

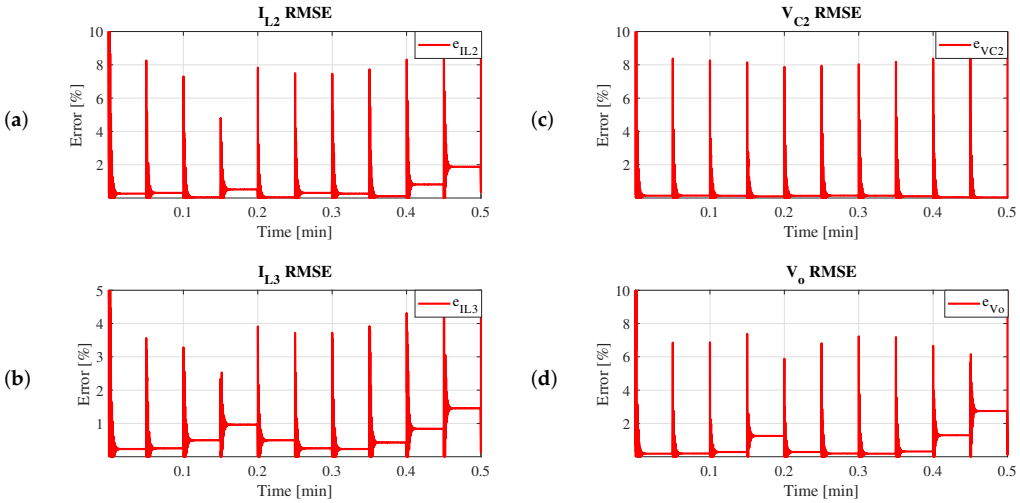


Figure 17. For the data−driven identified model, error between simulated and estimated signals: (**a**) inductor current I_{L2}, (**b**) inductor current I_{L3}, (**c**) capacitor voltage V_{C2}, and (**d**) capacitor voltage V_o.

To verify the accuracy of the model under conditions different from those used for its identification, Figure 17 shows the RMSE error for currents $I_{L_{2,3}}$, (a) and (b), and those related to voltages V_{C_2} and V_o, (c) and (d). The magnitude of these errors does not exceed an average of 1% during steady-state periods. However, it can be observed that during transients, due to changes in the input signal d, errors of up to 10% are reached. This is because the transient response in the estimated signal from the data-based model is practically negligible.

6. Conclusions

This article proposes a data-driven methodology to determine a model for DC–DC power electronic converters based on state–space representation without the need for an equivalent electrical model and requiring only a few measurements. Additionally, it enables the identification of matrices **A**, **B**, **C**, and **D**, which define a linear dynamic system. This methodology allows for the recognition of the system trajectories, which are determined by the coefficient matrix $\mathscr{R}$ through the application of controlled changes to the input signal d and the observation of output signals, including voltages and currents. This process establishes a system of linear difference equations that approximates the actual behavior of the converters.

Furthermore, in cases where access to one of the system variables is restricted or if there is a need to correct the state trajectories, an observer can be implemented to help adjust the system inputs, providing a more accurate estimation of the output variables.

The model validation was carried out using a different excitation condition for the input signal d than the one used for its identification and by comparing the model's output with simulation measurements. The error between the estimated and simulated signals for the converters ranges from 1% to 3% for the currents, while the average deviation between the model and the simulation is around 4% for the voltages in the comparison between models. On the other hand, for the verification of the generated models, an average deviation during steady-state conditions of no more than 1% was observed in all cases. The results showed that the trajectories of the analyzed converters from the generated model can closely follow the trajectories of the real system, providing a highly accurate estimation of the proposed voltages and currents for each converter.

Author Contributions: Conceptualization, G.E. and J.E.V.-R.; Methodology, D.G. and J.C.R.-C.; Validation, E.D.S.-V. and J.E.V.-R.; Formal analysis, E.D.S.-V. and J.E.V.-R.; Investigation, E.D.S.-V. and J.M.S.; Writing, E.D.S.-V., G.E., J.E.V.-R. and J.C.R.-C.; Review and editing, D.G., J.M.S., G.E. and J.C.R.-C. All authors have read and agreed to the published version of the manuscript.

Funding: This research and the APC was funded in part by CONAHCYT, grant number CF-2023-G-1344, and Tecnológico de Monterrey.

Data Availability Statement: Data are contained within the article.

Acknowledgments: The authors would like to thank CONAHCYT for their support through the project CF-2023-G-1344 Desarrollo de nuevos enfoques para analisis, modelado y control de convertidores electronicos. Also, we want to thank Universidad Panamericana for the APC support.

Conflicts of Interest: The authors declare no conflicts of interest.

Nomenclature

The following abbreviations are used in this manuscript:

Δd	Duty cycle variation
d	Duty cycle
I_{L_x}	Inductor current
$\mathscr{R}$	Coefficient Matrix
R_L	Resistive Load
R_{L_x}	Inductor parasitic resistance
$RMSE$	Root Mean Squared Error
$V_{C_{nx}}$	Capacitor voltage
V_{in}	Input voltage
V_o	Output voltage

References

1. Singh, A.K.; Mishra, A.K.; Gupta, K.K.; Siwakoti, Y.P. High voltage gain bidirectional DC-DC converters for supercapacitor assisted electric vehicles: A review. *CPSS Trans. Power Electron. Appl.* **2022**, *7*, 386–398. [CrossRef]
2. Aravind, R.; Bharatiraja, C.; Verma, R.; Aruchamy, S.; Mihet-Popa, L. Multi-Port Non-Isolated DC-DC Converters and their Control Techniques for the Applications of Renewable Energy. *IEEE Access* **2024**, *12*, 88458–88491. [CrossRef]
3. Kazimierczuk, M.K. *Pulse-Width Modulated DC-DC Power Converters*; John Wiley & Sons: Hoboken, NJ, USA, 2015.
4. Luo, F.L.; Ye, H. *Advanced DC-DC Converters*; CRC Press: Boca Raton, FL, USA, 2016.
5. Mostaan, A.; Gorji, S.A.; Soltani, M.; Ektesabi, M. A novel quadratic buck-boost DC-DC converter without floating gate-driver. In Proceedings of the 2016 IEEE 2nd Annual Southern Power Electronics Conference (SPEC), Auckland, New Zealand, 5–8 December 2016; pp. 1–5. [CrossRef]
6. Carstensen, C.; Biela, J. A Three-Level Buck Converter with a Wide Voltage Operation Range for Hardware-in-the-Loop Test Systems. *IEEE Trans. Power Electron.* **2016**, *31*, 6176–6191. [CrossRef]
7. Cervero, D.; Fotopoulou, M.; Muñoz-Cruzado, J.; Rakopoulos, D.; Stergiopoulos, F.; Nikolopoulos, N.; Voutetakis, S.; Sanz, J.F. Solid state transformers: A critical review of projects with relevant prototypes and demonstrators. *Electronics* **2023**, *12*, 931. [CrossRef]
8. Haro-Larrode, M.; Bayod-Rújula, Á.A. A coordinated control hybrid MPPT algorithm for a grid-tied PV system considering a VDCIQ control structure. *Electr. Power Syst. Res.* **2023**, *221*, 109426. [CrossRef]
9. Rosas-Caro, J.C.; Valdez-Resendiz, J.E.; Escobar, G.; Beltran-Carbajal, F. A Multilevel Boost Converter with Reduced Inductor Current. *Electronics* **2023**, *12*, 4585. [CrossRef]
10. Zhang, J.; Yang, X.; Chen, W.; Zhou, H.; Luo, J. A multifrequency small-signal model for the MLCL-filtered grid-connected inverter considering the FCE of nonlinear inductors. *IEEE Trans. Ind. Electron.* **2022**, *70*, 4901–4911. [CrossRef]
11. Long, B.; Hu, C.; Chen, Z.; Hu, J.; Rodríguez, J.; Zang, X. Fractional-Order Sequential Model Predictive Control of Three-Phase Fractional-Order T-Type Converters. *IEEE J. Emerg. Sel. Top. Power Electron.* **2023**, *11*, 5820–5832. [CrossRef]
12. Pacheco-Cherrez, D.S.; Guillen, D.; Mayo-Maldonado, J.C.; Escobar, G. Data-Driven Optimal Voltage Performance Index Tracking in Active Distribution Networks. *IEEE Trans. Smart Grid* **2024**, *15*, 4804–4818. [CrossRef]
13. Rahman, A.U.; Syed, I.; Ullah, M. Small-signal stability criteria in AC distribution systems—A review. *Electronics* **2019**, *8*, 216. [CrossRef]
14. Behjati, H.; Niu, L.; Davoudi, A.; Chapman, P.L. Alternative time-invariant multi-frequency modeling of PWM DC-DC converters. *IEEE Trans. Circuits Syst. I Regul. Pap.* **2013**, *60*, 3069–3079. [CrossRef]
15. Yue, X.; Wang, X.; Blaabjerg, F. Review of small-signal modeling methods including frequency-coupling dynamics of power converters. *IEEE Trans. Power Electron.* **2018**, *34*, 3313–3328. [CrossRef]
16. Wang, L.; Deng, X.; Han, P.; Qi, X.; Wu, X.; Li, M.; Xu, H. Electromagnetic transient modeling and simulation of power converters based on a piecewise generalized state space averaging method. *IEEE Access* **2019**, *7*, 12241–12251. [CrossRef]
17. Azer, P.; Emadi, A. Generalized state space average model for multi-phase interleaved buck, boost and buck-boost DC-DC converters: Transient, steady-state and switching dynamics. *IEEE Access* **2020**, *8*, 77735–77745. [CrossRef]

18. Lei, J.; Xiang, X.; Li, W.; He, X. The analysis and calculation of power angle dynamics in grid forming converter under large disturbances based on KBM asymptotic method. *IEEE Trans. Power Electron.* **2022**, *38*, 1494–1508. [CrossRef]
19. Bernal, C.; Oyarbide, E.; Gaudo, P.M.; Mediano, A. Dynamic model of class-E inverter with multifrequency averaged analysis. *IEEE Trans. Ind. Electron.* **2012**, *59*, 3737–3744. [CrossRef]
20. Leng, M.; Zhou, G.; Tian, Q.; Xu, G.; Zhang, X. Improved small-signal model for switching converter with ripple-based control. *IEEE Trans. Ind. Electron.* **2020**, *68*, 222–235. [CrossRef]
21. Tian, S.; Lee, F.C.; Li, Q.; Yan, Y. Unified equivalent circuit model and optimal design of v^2 controlled buck converters. *IEEE Trans. Power Electron.* **2015**, *31*, 1734–1744. [CrossRef]
22. Lv, Z.; Zhou, M.; Wang, Q.; Hu, W. Small-signal stability analysis for multi-terminal LVDC distribution network based on distributed secondary control strategy. *Electronics* **2021**, *10*, 1575. [CrossRef]
23. Deraz, S.A.; Zaky, M.S.; Tawfiq, K.B.; Mansour, A.S. State Space Average Modeling, Small Signal Analysis, and Control Implementation of an Efficient Single-Switch High-Gain Multicell Boost DC-DC Converter with Low Voltage Stress. *Electronics* **2024**, *13*, 3264. [CrossRef]
24. Meng, X.; Hu, G.; Liu, Z.; Wang, H.; Zhang, G.; Lin, H.; Sadabadi, M.S. Neural Network-Based Impedance Identification and Stability Analysis for Double-Sided Feeding Railway Systems. *IEEE Trans. Transp. Electrif.* **2024**, 1. [CrossRef]
25. Shafaei, R.; Ordonez, M.; Saket, M.A. Three-dimensional frequency-dependent thermal model for planar transformers in LLC resonant converters. *IEEE Trans. Power Electron.* **2018**, *34*, 4641–4655. [CrossRef]
26. Nabinejad, A.; Rajaei, A.; Mardaneh, M. A systematic approach to extract state-space averaged equations and small-signal model of partial-power converters. *IEEE J. Emerg. Sel. Top. Power Electron.* **2019**, *8*, 2475–2483. [CrossRef]
27. Shankaran, G.V.; Dogruoz, M.B.; Abarham, M. Thermal Analysis and Design of Electronics Systems across Scales Using State-Space Modeling Technique. *IEEE Trans. Compon. Packag. Manuf. Technol.* **2021**, *11*, 1223–1234. [CrossRef]
28. Vargas, U.; Ramirez, A. Reformulating extended harmonic domain models for accurate representation of harmonics dynamics. *IEEE Trans. Power Deliv.* **2016**, *31*, 2562–2564. [CrossRef]
29. Wang, K.; Wu, F.; Su, J. Harmonic State-Space Modeling and Closed-Loop Control of Single-Stage High-Frequency Isolated DC–AC Converter. *IEEE Trans. Ind. Electron.* **2023**, *71*, 4576–4585. [CrossRef]
30. Daryabak, M.; Filizadeh, S.; Jatskevich, J.; Davoudi, A.; Saeedifard, M.; Sood, V.; Martinez, J.; Aliprantis, D.; Cano, J.; Mehrizi-Sani, A. Modeling of LCC-HVDC systems using dynamic phasors. *IEEE Trans. Power Deliv.* **2014**, *29*, 1989–1998. [CrossRef]
31. Bi, T.; Liu, H.; Feng, Q.; Qian, C.; Liu, Y. Dynamic phasor model-based synchrophasor estimation algorithm for M-class PMU. *IEEE Trans. Power Deliv.* **2015**, *30*, 1162–1171. [CrossRef]
32. Almozayen, M.A.; Knight, A.M. Dynamic phasor finite element modeling of grid-connected DFIG considering winding space harmonics. *IEEE Access* **2022**, *10*, 65913–65924. [CrossRef]
33. Motwani, J.K.; Xue, Y.; Nazari, A.; Dong, D.; Cvetkovic, I.; Boroyevich, D. Modeling of power electronics systems and PWM modulators in harmonic-state space. *IEEE Open J. Power Electron.* **2022**, *3*, 689–704. [CrossRef]
34. Xu, Z.; Li, B.; Wang, S.; Zhang, S.; Xu, D. Generalized single-phase harmonic state space modeling of the modular multilevel converter with zero-sequence voltage compensation. *IEEE Trans. Ind. Electron.* **2018**, *66*, 6416–6426. [CrossRef]
35. Li, Y.; Sun, Y.; Li, K.J.; Lou, J.; Sun, K.; An, P. Harmonic Power Flow Calculation Based on Unified Harmonic State-Space Model of Converter. In Proceedings of the 2022 IEEE Industry Applications Society Annual Meeting (IAS), Detroit, MI, USA, 9–14 October 2022; IEEE: Piscataway, NJ, USA, 2022; pp. 1–7.
36. Escobar, G.; Mayo-Maldonado, J.C.; del Puerto-Flores, D.; Valdez-Resendiz, J.E.; Micheloud, O.M. A Single-Phase Globally Stable Frequency-Locked Loop Based on the Second-Order Harmonic Oscillator Model. *Electronics* **2021**, *10*, 525. [CrossRef]
37. Wang, L.; Zhang, J. Methodology for Improving High-Power Harmonic Measurement Accuracy and Stability. *Electronics* **2022**, *11*, 3808. [CrossRef]
38. Zhu, S.; Liu, J.; Cao, Y.; Guan, B.; Du, X. Vienna Rectifier Modeling and Harmonic Coupling Analysis Based on Harmonic State-Space. *Electronics* **2024**, *13*, 1447. [CrossRef]
39. Meng, X.; Liu, Z.; Liu, Y.; Zhou, H.; Tasiu, I.A.; Lu, B.; Gou, J.; Liu, J. Conversion and SISO equivalence of impedance model of single-phase converter in electric multiple units. *IEEE Trans. Transp. Electrif.* **2022**, *9*, 1363–1378. [CrossRef]
40. Rapisarda, P.; Willems, J.C. State maps for linear systems. *SIAM J. Control Optim.* **1997**, *35*, 1053–1091. [CrossRef]
41. Balakrishnan, V. *System Identification: Theory for the User: Lennart Ljung*; Prentice-Hall: Englewood Cliffs, NJ, USA, 1999; ISBN 0-13-656695-2.
42. Rivera, D.; Guillen, D.; Mayo-Maldonado, J.C.; Valdez-Resendiz, J.E.; Escobar, G. Power grid dynamic performance enhancement via statcom data-driven control. *Mathematics* **2021**, *9*, 2361. [CrossRef]
43. Willems, J.C.; Rapisarda, P.; Markovsky, I.; De Moor, B.L. A note on persistency of excitation. *Syst. Control Lett.* **2005**, *54*, 325–329. [CrossRef]
44. Warren, J.R.; Rosowski, K.A.; Perreault, D.J. Transistor selection and design of a VHF DC-DC power converter. *IEEE Trans. Power Electron.* **2008**, *23*, 27–37. [CrossRef]
45. Zhang, J.; Chung, C.; Guan, L. Noise effect and noise-assisted ensemble regression in power system online sensitivity identification. *IEEE Trans. Ind. Inform.* **2017**, *13*, 2302–2310. [CrossRef]

46. Tan, A.H.; Godfrey, K.R.; Barker, H.A. Design of ternary signals for MIMO identification in the presence of noise and nonlinear distortion. *IEEE Trans. Control Syst. Technol.* **2009**, *17*, 926–933. [CrossRef]
47. Sosa, J.M.; Escobar, G.; Martínez-Rodríguez, P.R.; Vázquez, G.; Juárez, M.A.; Nava-Cruz, J.C. A model-based controller for a DC-DC boost converter with an LCL input filter. In Proceedings of the IECON 2015-41st Annual Conference of the IEEE Industrial Electronics Society, Yokohama, Japan, 9–12 November 2015; IEEE: Piscataway, NJ, USA, 2015; pp. 619–624.

Disclaimer/Publisher's Note: The statements, opinions and data contained in all publications are solely those of the individual author(s) and contributor(s) and not of MDPI and/or the editor(s). MDPI and/or the editor(s) disclaim responsibility for any injury to people or property resulting from any ideas, methods, instructions or products referred to in the content.